

Beyond binarity in A stars

II. Disentangling the four stars in the vicinity of the triple HIP 87813 within the quintuple system HJ2814 *

Idel Waisberg¹, Ygal Klein¹ and Boaz Katz¹

Department of Particle Physics and Astrophysics, Weizmann Institute of Science, Rehovot 76100, Israel; e-mail: idel.waisberg@weizmann.ac.il

April 20, 2022

ABSTRACT

A-stars are the progenitors of about half of the white dwarfs (WDs) that currently exist. The connection between the multiplicity of A-stars and that of WDs is not known and both multiplicities are still poorly explored. We are in the process of obtaining tight constraints on a sample of 108 southern A-type stars that are part of the nearby VAST sample (De Rosa et al. 2014) by conducting near-infrared interferometric follow-up observations to the (twenty) stars among them which have large *Gaia-Hipparcos* accelerations. In this paper, we combine spectroscopy, adaptive optics imaging, NIR interferometry and *Gaia-Hipparcos* astrometry in order to disentangle the stars in the complicated HIP 87813 = HJ2814A system. We show that (i) a previously discovered faint star that is separated by 2'' from the A star is actually a background source; (ii) the *Gaia-Hipparcos* acceleration is caused by a newly discovered $0.74M_{\odot}$ star that was missed in previous AO images and we solve for its $P \approx 60$ yrs astrometric orbit; (iii) by combining previously obtained spectra we show that the A star has a very close $0.85M_{\odot}$ companion on a 13.4-day period orbit. The radial velocity curve combined with NIR interferometry constrains its orbit allowing Kozai-Lidov oscillations in the hierarchical triple to be ruled out. The system HJ2814 is one of only about fifteen known 5+ systems with an A star primary, and will result in a system of between two to five bound WDs within around a Hubble time.

Key words. stars: multiple – stars: kinematics and dynamics – techniques: interferometric – stars: individual (HIP 87813)

1. Introduction

Multiple star systems are important in the study of star formation, interaction dynamics and the ultimate fate of stars. Systems containing one or more A stars are particularly interesting as these stars evolve within the age of the Universe to form white dwarfs (WDs), and are among the main progenitors of the WDs we see today. WDs in multiple systems are in turn believed to be the progenitors of type Ia Supernovae (e.g. Hillebrandt & Niemeyer 2000; Maoz et al. 2014). However, the multiplicity of A stars is comparatively less studied than that of lower and more massive stars, and is not well known (e.g. Duchêne & Kraus 2013; Moe & Di Stefano 2017).

De Rosa et al. (2014) recently analyzed an adaptive optics (AO) survey of 363 (photometrically selected) A-stars within 75 pc (VAST survey), providing a complete census of most companions at separations $0.3'' \lesssim \rho \lesssim 10''$. *Gaia* EDR3 (*Gaia* Collaboration et al. 2021; Lindegren et al. 2021), on the other hand, allows the detection of most main sequence (MS) companions at separations $\gtrsim 5''$ by identifying common proper motion (CPM) pairs (note that the VAST survey includes a CPM search but is superseded by *Gaia*). Binaries at separations \lesssim few AU are

in principle accessible to photometric (e.g. Murphy et al. 2018) or spectroscopic techniques with radial velocity measurements (limited to small separations due to the large width of the spectral lines of the rotating A stars), albeit such observations are highly demanding. An important knowledge gap remains for separations $0.01'' \lesssim \rho \lesssim 0.3''$ ($1 \text{ AU} \lesssim a \lesssim 20 \text{ AU}$ for a distance $d = 75 \text{ pc}$). Intermediate mass binaries in this separation range are, however, likely common (e.g. Klein & Katz 2017). In fact, 4 of the closest 6 known WDs (Sirius B, Procyon B, 40 Eridani B and Stein 2051 B, all within 6 pc) have MS companions within $10 \text{ AU} < a < 50 \text{ AU}$, and probably had progenitor systems consisting of an intermediate mass star in a MS-MS binary with $1 \text{ AU} \lesssim a \lesssim 30 \text{ AU}$ separation.

Missing stars in the separation range of $\sim 10 \text{ AU}$ may significantly affect our estimates of high multiplicity beyond binarity, with three or more components. High multiplicity is particularly challenging to infer and almost always requires a combination of different techniques – including imaging, lightcurves, radial velocity curves, astrometry and interferometry – which have different sensitivities and biases to orbital separation, inclination and companion contrast. While high (3+) multiplicity is very common among massive stars (e.g. Sana et al. 2014), the fraction of F and G dwarfs in high multiplicity (3+) systems appears to be much lower, on the order of 10% (e.g. Tokovinin 2014). This gap calls for a better understanding of the multiplicity of

* Based on observations collected at the European Southern Observatory, Chile, Program IDs 075.D-0342, 077.D-0164, 093.D-0346, 105.20RL.001

A stars as progenitors of systems containing one or more WDs. High multiplicity may play an important role in the evolution of the system before, during or after stellar evolution (e.g. Harrington 1968; Kiseleva et al. 1998; Tokovinin et al. 2006; Fabrycky & Tremaine 2007; Perets & Fabrycky 2009; Toonen et al. 2016; Hamers et al. 2021; Gao et al. 2022) and may affect the prospects of the system to result in a type Ia supernovae (e.g. Thompson 2011; Katz & Dong 2012; Kushnir et al. 2013).

We are in the process of obtaining tight constraints on a volume limited sample of 108 nearby ($40 \text{ pc} \lesssim d \lesssim 80 \text{ pc}$) southern A-type stars that are part of the VAST sample by conducting near-infrared interferometric followup observations to the (twenty) stars among them that show a large proper motion change $\Delta \text{PM} > 0.5 \text{ km s}^{-1}$ between *Hipparcos* and *Gaia* (based on Brandt 2018, 2021, indicative of a nearby $M \gtrsim 1 M_{\odot}$ companion). In addition to the prospects of identifying the companion/s causing the acceleration (in the many cases in which a suitable companion was not detected in the AO images), the interferometry provides constraints on the 3d orientation of the close (e.g. spectroscopic) binaries, which is crucial to assess the dynamical state of the system. For a more detailed description of the survey, we refer to Paper I of this series.

In this paper, we present new observations and analysis of one of these A stars, HIP 87813 = HJ 2814A which demonstrates the challenges and potential of combining astrometric, spectroscopic, AO and interferometric observations for studying multiplicity. HIP 87813 is an interesting example for which the *Gaia* – *Hipparcos* acceleration is too large to be explained by the previously identified close companion at $2''$. By reanalysing previous AO images we find a new close companion which accounts for the *Gaia* – *Hipparcos* acceleration and show that the previously identified close companion is a background star. By analysing previous spectroscopic observations we confirm the existence of an additional, previously suspected tight companion making HJ 2814A a triple system. By combining the imaging, spectroscopic, astrometric and new and archival interferometric observations we solve for the inner and outer orbits and put tight constraints on their orientation and possible dynamics. The entire HJ 2814 system, which includes a (previously known) common proper motion binary HJ 2814B is thus a quintuple system (see Figure 1). This paper is structured as follows. Section 2 summarizes the properties of the system known prior to our analysis and the astrometric data from different surveys. Section 3 describes the archival and new observations and the data reduction. Section 4 presents the direct results, which are put together and further analyzed in Section 5 to reveal a consistent picture for HIP 87813. Finally, we discuss in Section 6 the ongoing dynamical processes in the system, as well as its possible formation scenarios and its future evolution.

2. HJ 2814 HIP 87813

We show in Figure 1 the multiplicity structure of HJ 2014, including the previously known and the newly discovered components, which will be discussed throughout this paper.

HIP 87813 is part of HJ 2814, which consists of two main components separated by $20.6''$, which translates to a physical projected separation of 1617 AU using the *Gaia* eDR3 (Gaia Collaboration et al. 2021) distance of $d = 78.2 \text{ pc}$ for

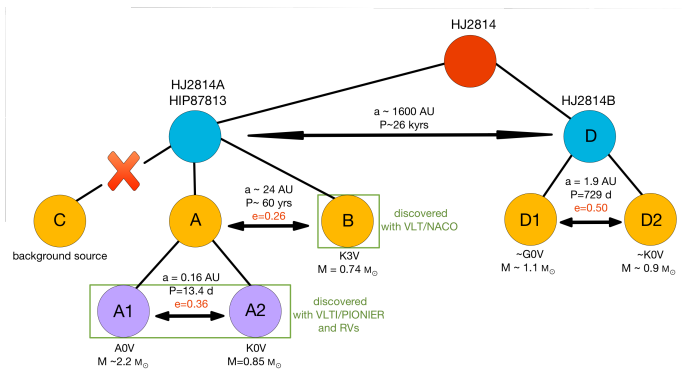


Fig. 1. Multiplicity schematic for HJ2814 combining the previously known information and the new discoveries in this paper.

HIP 87813 (Bailer-Jones et al. 2021). The association is extremely likely to be physical given the consistent parallaxes and close proper motions of the two objects in *Gaia* eDR3.

The fainter component HJ 2814B (=BD-15 4723) is a double line spectroscopic binary (D=D₁+D₂ in Figure 1) with a period $P = 729$ days and eccentricity $e = 0.5$ (Tokovinin 2019). The color and luminosity of this component correspond to a G0V star, and the mass ratio inferred from the RV curves is 0.82. Therefore, the system consists roughly of an early G and an early K type main sequence (MS) stars with a semi-major axis of about 1.9 AU.

HJ 2814A, also known as HIP 87813, is the topic of this paper and is an A0-1V star. Using multi-band photometry, Zorec & Royer (2012) estimated its fundamental parameters: effective temperature $T_{\text{eff}} = 9290 \pm 150 \text{ K}$ and luminosity $L = 23.8 \pm 1.8 L_{\odot}$ ($R = 1.9 \pm 0.1 R_{\odot}$). Using evolutionary tracks on the HR diagram they then estimated a mass $M = 2.14 \pm 0.03 M_{\odot}$ and a fractional age on the main sequence $t/t_{\text{MS}} = 0.276 \pm 0.086$ (corresponding to an age around $t \sim 400$ Myrs). De Rosa et al. (2014) also estimated a mass and age for the star by comparing the NIR K band magnitude and the $V - K$ color with theoretical isochrones, finding similar values of $M = 2.11 M_{\odot}$ and $t = 350$ Myrs. The projected rotational velocity of the A star is reported as $v \sin i = 52 \text{ km/s}$ in Glebocki & Gnacinski (2005) and $v \sin i = 60 \text{ km/s}$ in Royer et al. (2007).

A probable binary nature for this star was noted in Tokovinin (2019) based on three different radial velocities reported in Nordstrom & Andersen (1985) and on a large proper motion change between *Hipparcos* and *Gaia* DR2 (Gaia Collaboration et al. 2018). Based on this, the system HJ 2814 is classified as a quadruple in the most recent version of the Multiple Star Catalogue (Tokovinin 2018). The fact that the radial velocities changed by 30 km s^{-1} over four days, however, suggests a short-period orbit that cannot explain the proper motion change, and already hint towards at least a triple star nature for HIP 87813.

Furthermore, De Rosa et al. (2014) reported the discovery of a faint companion to the A star at a projected separation $\rho = 1.88''$ based on archival AO observations with VLT/NACO. From the contrast in K band magnitude $\Delta K = 6.66$ and assuming the stars are physically related, they estimated the companion mass to be $0.17 M_{\odot}$, corresponding to a mid to late M dwarf. This putative companion, however, can explain neither the radial velocity nor the proper motion changes of the A star.

1. Astrometry of HIP 87813

In table 1 we collect the proper motions of HIP 87813 as given by the FOCAT-S catalogue (Bystrov et al. 1994), *Hipparcos* (van Leeuwen 2007), *Gaia* DR2 (Gaia Collaboration et al. 2018) and *Gaia* eDR3 (Gaia Collaboration et al. 2021), with mean epochs J1982.492, J1991.25, J2015.5 and J2016.0 respectively. The FOCAT-S proper motion is based on two position measurements but the individual epochs are not reported. The *Hipparcos*, *Gaia* DR2 and *Gaia* eDR3 positions and proper motions are based on 82, 147 and 167 measurements made over a few years. We also show the “effective” proper motion based on the positional difference between *Gaia* (DR2) and *Hipparcos* (e.g. Brandt 2018, 2021), which is much more precise than the individual proper motions. These values were translated to km s^{-1} using a geometric distance $d = 78.2$ pc based on the *Gaia* eDR3 parallax (Bailer-Jones et al. 2021).

There is a significant change in both the short-term proper motions measured by *Hipparcos* and *Gaia* DR2 ($|\Delta\text{PM}| = \sqrt{(\text{PM}_{\text{RA}})^2 + (\text{PM}_{\text{DEC}})^2} = 3.90 \pm 0.33 \text{ km s}^{-1}$) as well as between *Gaia* DR2 and the effective proper motion based on the positional difference between *Gaia* DR2 and *Hipparcos* ($|\Delta\text{PM}| = 1.24 \pm 0.07 \text{ km s}^{-1}$). On the other hand, there is no significant proper motion change between *Gaia* DR2 and eDR3 ($|\Delta\text{PM}| = 0.07 \pm 0.08 \text{ km s}^{-1}$). This suggests that the acceleration is caused by an orbit with a period $P \gg 1$ yr.

On the other hand, *Gaia* eDR3 reports both a high astrometric noise of 0.62 mas (with a significance of 277) and a high RUWE (Renormalized Unit Weight Error) parameter (Lindgren et al. 2021) of 2.84 for HIP87813. These are both indications that the single-star solution is very poor and that the star is possibly a multiple (e.g. Belokurov et al. 2020). Since there is no change in proper motion between DR2 and eDR3, the astrometric noise is likely to be caused by a very short period ($P \ll 1$ yr) binary whose orbit averages out in the measurement of the *Gaia* proper motions, rather than by a residual from the acceleration caused by the long period binary.

The astrometric data therefore provides further evidence that the A star in HIP 87813 is actually at least a triple system, the nature of which can be elucidated with the radial velocity, imaging and interferometric observations that will be presented below.

3. Observations and data reduction

1. Spectra

We collected FEROS spectra of HIP87813 from the ESO Phase 3 archive¹. FEROS (Kaufer et al. 1999) is an Echelle spectrograph mounted on the MPG/ESO 2.2-m telescope in ESO La Silla observatory, Chile. The instrument covers the wavelength region 3500-9200 Å at high spectral resolution ($R \approx 48000$). The observations of HIP87813 were carried out on 2005-05-26 (8 integrations throughout 9 hours), 2005-05-27 (7 integrations throughout 7 hours), 2005-05-28 (two integrations separated by 2 hours) and 2006-06-29 (4 observations throughout 3 hours). The integration times varied between 240 and 600 seconds. We downloaded the spectra fully reduced and calibrated. We note that in the

¹ http://archive.eso.org/wdb/wdb/adp/phase3_main/form?collection_name=FEROS

phase 3 spectra the wavelengths are in air and are already corrected to the heliocentric frame.

We also collected spectra of HIP87813 from the NASA’s Infrared Telescope Facility (IRTF) archive², which collects and organizes observations from 2016. IRTF harbors a 3-m telescope optimized for infrared astronomy and located in Mauna Kea observatory in Hawaii. Being an A0V star, HIP 87813 was often observed as a telluric calibrator for several different programs. We downloaded the raw data and calibration files for observations with the medium resolution spectrograph SpeX (Rayner et al. 2003). We retrieved the observations with the SXD grating (covering $0.7 - 2.5 \mu\text{m}$ with resolution $R \sim 2000$) or, if it did not exist, with the LXD long grating (covering $2 - 5.3 \mu\text{m}$ with resolution $R \sim 2500$). The total exposure times per observation are in the range of 1 – 10 seconds. We reduced the data using the publicly available pipeline *Spextool* (Cushing et al. 2004), which includes flat fielding, wavelength calibration, order extraction and merging. We note that the resulting IRTF spectra are in vacuum wavelengths.

2. AO imaging

From the ESO archive, we collected three epochs of NIR AO observations of HIP87813 taken with NAOS-CONICA (NACO; Lenzen et al. 2003; Rousset et al. 2003) when it was mounted on the 8.2-m telescope UT4 of the Very Large Telescope (VLT) at ESO Paranal, Chile. The details of the observations are listed in Table 2. All images were obtained in the K_s band with the S27 camera, which provides a $28'' \times 28''$ field of view with a 27 mas pixel^{-1} scale. In addition, a neutral density filter (“ND short”) which reduces the flux by a factor of 80 was used in order to avoid saturation of the detector. The nearby star 2MASS 17564161-1551076 was used as a natural guide star for the AO corrections.

We reduced the data with the standard ESO NACO pipeline version 4.4.9 following the standard steps of dark subtraction, flat fielding using twilight sky frames and co-adding all the images. The FWHM of the resulting Point Spread Function (PSF), measured by fitting a two-dimensional Gaussian to the star, is about 110 mas in all three images.

3. NIR interferometry

3.1. VLTI/PIONIER

HIP 87813 was observed with the beam combiner instrument PIONIER (Le Bouquin et al. 2011) at the Very Large Telescope Interferometer (VLTI) in ESO Paranal on August 26th, 2014, as a calibrator star for the program 093.D-0346 (PI: Schoeller). It was observed in the one spectral channel mode (“H FREE”), with central wavelength $1.681 \mu\text{m}$ and bandwidth $0.245 \mu\text{m}$, in two different sets of 5 recordings separated by 1h30min within the night with average seeing conditions. Each recording is a 30s exposure containing 100 interferograms. Each set provides six squared visibilities (V^2) for each of the six baselines and four closure phases (ϕ_3) for each of the four telescope triangles. Therefore, the entire observations comprise twelve squared visibilities and eight closure phases. The observations were made using the four 1.8-m Auxiliary Telescopes (ATs) in the station con-

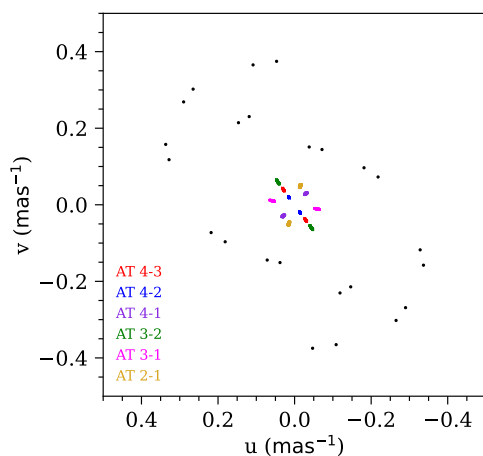
² <https://irsa.ipac.caltech.edu/applications/irtf/>

Table 1. Proper motion measurements of HIP 87813.

source	epoch	pmra	pmdec
		(mas yr ⁻¹) (km s ⁻¹)	(mas yr ⁻¹) (km s ⁻¹)
FOCAT-S	J1982.492	-5 ± 1 -1.9 ± 0.4	-63 ± 5 -23.4 ± 1.9
<i>Hipparcos</i>	J1991.25	-9.77 ± 0.50 -3.62 ± 0.19	-65.32 ± 0.30 -24.23 ± 0.11
<i>Gaia</i> DR2	J2015.5	-1.44 ± 0.20 -0.53 ± 0.07	-72.79 ± 0.16 -27.00 ± 0.06
<i>Gaia</i> eDR3	J2016.0	-1.60 ± 0.11 -0.59 ± 0.04	-72.68 ± 0.07 -26.96 ± 0.03
<i>Gaia</i> DR2 - <i>Hipparcos</i>	-	-4.44 ± 0.02 -1.647 ± 0.009	-71.36 ± 0.02 -26.469 ± 0.007

Table 2. Summary of archival NACO observations.

Date	DIT (sec)	integration time (sec)	seeing @ 500 nm (")
2004-06-27	2.5	450	1.3-1.5
2006-04-28	1	336	1.6-2.4
2006-05-19	4	588	1.4


Fig. 2. uv coverage of VLTI observations of HIP 87813. The black points correspond to the PIONIER observations and the colorful points to the GRAVITY observations.

figuration A1-G1-J3-K0, which provided a maximum projected baseline length of 140 meters, corresponding to an angular resolution of 2.5 mas (we note that structures up to a few times smaller than the maximum resolution can be partially resolved). The resulting uv -coverage is shown in Figure 2. A summary of the observations is reported in Table 3.

We note that HIP 87813 was observed as an interferometric calibrator which, in principle, would make it im-

possible to extract scientific information from its observations if they were isolated (we note that the fact, as will be shown below, that HIP 87813 is not a single star would make it inappropriate as an interferometric calibrator, a misfortune that sometimes happens in optical/NIR interferometry). Luckily, however, the observations were part of a very long sequence of homogeneous PIONIER observations including several targets throughout the night; therefore, it was possible to use another (true) calibrator star and treat HIP 87813 as a scientific target. In this case, we chose the calibrator HD 158352, which was observed within 15 min of HIP 87813 and with the same instrumental setup, and whose details are shown in Table 4. Although the on-sky distance between the two stars is larger ($\approx 17.5^\circ$) than would typically be selected for an interferometric calibrator ($\lesssim 3^\circ$), we found that the systematic calibration errors – which for canonical observations with PIONIER are around 3% for V^2 and 2° for ϕ_3 (Le Bouquin et al. 2011) – are still small enough to allow the data to be useful, albeit with a larger error in the calibrated squared visibilities.

We downloaded the data from the ESO archive, including the calibration files (dark and kappa matrix frames), and reduced the data using the default settings in the PIONIER data reduction software `pndrs` v3.94 (Le Bouquin et al. 2011) downloaded from the Jean-Marie Mariotti Center (JMMC) website. The only additional step needed was to change the label of the observations of HIP 87813 from calibrator to science for the final calibration step.

Table 3. Summary of archival PIONIER and obtained GRAVITY interferometric observations.

instrument	date time(UTC)	avg.seeing @ 500 nm (")	avg.coherence time @ 500 nm (ms)	AT configuration	calibrator
PIONIER	2014-08-26 00:30-00:32	0.75	2	A1-G1-J3-K0	HD 158352
PIONIER	2014-08-26 02:09-02:12	1.00	1.5	A1-G1-J3-K0	HD 158352
GRAVITY	2021-09-02 02:17-02:36	0.74	3.6	A0-B2-D0-C1	HD 163449

Table 4. Interferometric calibrators.

calibrator	spectral				
	type	V	H	K	$\theta_{H/K}$ (mas)
HD 158352	A8V	5.4	4.9	4.8	0.41 ± 0.01^a
HD 163449	K0III	7.6	4.9	4.7	0.56 ± 0.01^a

Notes.

^(a) From the JMMC Stellar Diameter Catalog (JSDC) v2 (Bourges et al. 2017).

3.2. VLTI/GRAVITY

HIP 87813 was observed with the beam combiner instrument GRAVITY (Gravity Collaboration et al. 2017) on the VLTI on September 2nd, 2021, as one of the targets in our program to investigate the multiplicity of A stars that show large proper motion changes between *Hipparcos* and *Gaia*. GRAVITY operates in the NIR K band and the observations were made in single field mode: half of the light from the object was directed to the fringe tracker (FT), which operates in low spectral resolution mode ($R \approx 22$) in order to track and stabilize the fringes, while the other half was directed to the science (SC) channel, where coherent integrations of 30s were made in the high spectral resolution ($R \approx 4000$) mode. The observations were done in combined polarization mode and made use of the adaptive optics (AO) system NAOMI (Willez et al. 2019) using the optical light from the object itself. The total integration time on source was 16 min. The observations provided spectrally resolved squared visibilities and closure phases across the K band (1.97-2.40 μ m). The observations used the four ATs in the (“small”) configuration A0-B2-D0-C1, which provided a maximum projected baseline of 33 m, corresponding to an angular resolution of 12 mas. The resulting uv -coverage is shown in Figure 2. A summary of the observations is shown in Table 3. GRAVITY also records an 80 mas pixel⁻¹ H band image of 4" around the target every second for each telescope with its acquisition camera.

The data were reduced with the GRAVITY instrument pipeline v1.4.0 (Lapeyrere et al. 2014) downloaded from the ESO website. The star HD 163449 was used as an interferometric calibrator, and its properties are listed in Table 4.

4. Data analysis and direct results

1. Radial velocity measurements

We searched the VizieR online data catalogues and found four radial velocity measurements of HIP 87813: three in Nordstrom & Andersen (1985) (one from 1975 and two from 1977 separated by 4 days) and one in Grenier et al. (1999) (from 1994). These values already clearly show that it is an RV variable and are listed in Table A.1.

The FEROS spectra cover the blue optical region where strong and narrow metallic lines are particularly suitable for radial velocity measurements of A stars. We measure a radial velocity in each individual spectra by fitting a Gaussian profile to the strong and isolated CaII K line (rest wavelength 3933.663Å in air) using the `splot` routine in IRAF. The errors are calculated through a bootstrapping routine, with the flux errors estimated from the RMS in the adjacent continuum region. The resulting statistical RV errors vary from 20 – 260 m s⁻¹, and a clear change in RV within a single night can be seen. By finding the RMS dispersion between the eight (seven) observations in the first (second) nights after subtracting a linear fit, we find an RMS of 100 m s⁻¹, which is consistent with the estimated statistical errors. The individual RV measurements are listed in Table A.2.

We measure the radial velocity from the IRTF spectra by fitting a Lorentzian profile to the Pa β line (rest wavelength 12821.39Å in vacuum) or to the Br γ line (rest wavelength 21660.87Å) for the SXD and LXD long gratings, respectively. The statistical errors in the radial velocity measurements are on the order of 5 km s⁻¹; however, one might expect the errors to be systematic-dominated in this case because of the relatively low spectral resolution and the broad hydrogen lines. We use narrow telluric lines near the hydrogen lines in order to refine the wavelength calibration. Specifically, we use the telluric lines at 12688.50Å and 22001.59Å for the Pa β and Br γ lines, respectively, with their rest wavelength measured from the atmospheric transmission profile at spectral resolution $R = 2000$ provided in `Spextool`. We find corrections that vary between -50 and +68 km s⁻¹, and which are therefore crucial to be taken into account. Finally, we correct the velocities to the heliocentric frame using the function `rvcorrect` in IRAF. The individual RV measurements are listed in Table A.3.

The GRAVITY data taken at $R = 4000$ provides a K band spectrum from which a radial velocity can also be extracted. We averaged the spectrum from the four telescopes and for the four files, and found a velocity $v_z = -57 \pm 10$ km s⁻¹ by fitting a Lorentzian profile to

the Br γ line, and refining the wavelength calibration using the nearby telluric line as above. For reference, we note that the GRAVITY spectra returned by the pipeline are in vacuum wavelengths and not corrected to the heliocentric frame.

2. VLT/NACO images

Direct inspection of the AO NACO images showed not only the very faint star at 2" separation detected by De Rosa et al. (2014), but also another brighter companion in the halo of the A star. We speculate that the latter was missed by De Rosa et al. (2014) simply because the right contrast is needed in the image in order to make it clearly visible. From now on, we will refer to the A star, the close companion and the wider companion as A, B and C, respectively (see Figure 1). We plot the NACO images in Figure 3, with the left column highlighting the C component to the northeast and the middle column the B component to the (south)west. The latter has clearly moved northwards in around two years.

From the images we can measure the flux and position of B and C relative to A. While this is straightforward for component C, for component B PSF fitting is necessary because it is blended or sits in the halo of the much brighter A component. We experimented with a few different analytical models for the PSF, and found the best results with an elliptical Moffat profile (Moffat 1969). In this model the intensity of the source is

$$I(x, y) = (1 + A(x - x_0)^2 + B(y - y_0)^2) \quad (1)$$

$$+ C(x - x_0)(y - y_0)^{-\beta} \quad (2)$$

where (x_0, y_0) is the position of the source and

$$A = \frac{\cos(\theta)^2}{\alpha_x^2} + \frac{\sin(\theta)^2}{\alpha_y^2} \quad (3)$$

$$B = \frac{\sin(\theta)^2}{\alpha_x^2} + \frac{\cos(\theta)^2}{\alpha_y^2} \quad (4)$$

$$C = \sin(2\theta) \left(\frac{1}{\alpha_x^2} - \frac{1}{\alpha_y^2} \right) \quad (5)$$

where θ is the position angle of the ellipse and

$$\alpha_{x,y} = \frac{\text{FWHM}_{x,y}}{2\sqrt{2^{1/\beta} - 1}} \quad (6)$$

Together, $\alpha_{x,y}$ and β control the shape of the core and the wing of the PSF. In Table 5 we report the results of the PSF deblending for each of the three NACO epochs. In the right column of Figure 3, we plot the image with the best fit A component subtracted in order to highlight the B component. The residuals, which are particularly strong on the third image, are due to residual structure in the PSF not captured by the model. For the computation of the χ_{red}^2 , the errors were calculated by adding the estimated background and Poisson noise in quadrature. Component B is found to have a flux $6.2 \pm 0.2\%$ of component A (the first NACO epoch is the most reliable for the flux measurement since the blending is less severe).

The separation between the C and A components was measured by finding the centroid of the C component in the residual image, and are listed in Table 6. The flux ratio is consistent with $\Delta K = 6.7$ reported in De Rosa et al. (2014).

3. NIR interferometry

3.1. Binary model

For both PIONIER and GRAVITY, our basic model is that of a binary system with complex visibility (e.g. Waisberg 2019):

$$V = \frac{1 + f_c f e^{-2\pi j \mathbf{u} \cdot \boldsymbol{\sigma}}}{1 + f_c f} \quad (7)$$

where $0 < f < 1$ is the intrinsic binary flux ratio between the secondary and the primary in the observed band, \mathbf{u} is the uv coordinate and $\boldsymbol{\sigma}$ is the binary separation vector (which we parameterize as the separation ρ and the position angle PA (east of north) of the secondary relative to the primary). f_c is a fiber coupling constant that is important for very wide binaries and takes into account the attenuation of sources that are far away from the center of the fiber. We model it as

$$f_c = e^{-|\sigma|^2 / (2\sigma_{\text{fiber}}^2)} \quad (8)$$

where $\sigma_{\text{fiber}} = \text{FWHM}_{\text{fiber}}/2.355$ is the standard deviation of the fiber mode, which in the case of GRAVITY is matched to the Point Spread Function (PSF) of the telescope ($\text{FWHM}_{\text{fiber}} = 250$ mas in the case of the 1.8m ATs). Note that in Eq. 7 we assume that the fiber is centered on the primary star (which is an excellent approximation when $f \ll 1$). We also note that in Eq. 7:

1. We treat the stars as point sources because their size is much smaller than the interferometer resolution. For example, the A0V primary with a radius $R \approx 2R_{\odot}$ has an angular diameter $\theta \approx 0.2$ mas at its distance of $d = 78.2$ pc.
2. We neglect the effect of bandwidth smearing, which reduces the visibility for sources far from the center of the interferometric field of view $\text{FOV}_{\text{interf}} \sim 0.6 \frac{\lambda R}{B}$, where R is the spectral resolution and B the projected baseline. For our GRAVITY data taken at $R \approx 4000$, $\text{FOV}_{\text{interf}} \sim 30''$ for $\lambda = 2 \mu\text{m}$ and $B = 30$ m and this is a completely negligible effect. For the broadband PIONIER data with $R \approx 7$, this is a much more important effect since $\text{FOV}_{\text{interf}} \sim 15$ mas for $\lambda = 1.7 \mu\text{m}$ and $B = 100$ m; however, since we will be using the PIONIER data to explore the very close environment ($\lesssim 5$ mas) of the A star, we can neglect this effect as well. In practice, this means that the PIONIER observations are completely insensitive to component B.

4. VLTI/PIONIER

As detailed above, due to the bandwidth smearing effect the PIONIER data is completely insensitive to the component B (the possibility that the projected separation of the star has changed significantly due to a high eccentricity and/or

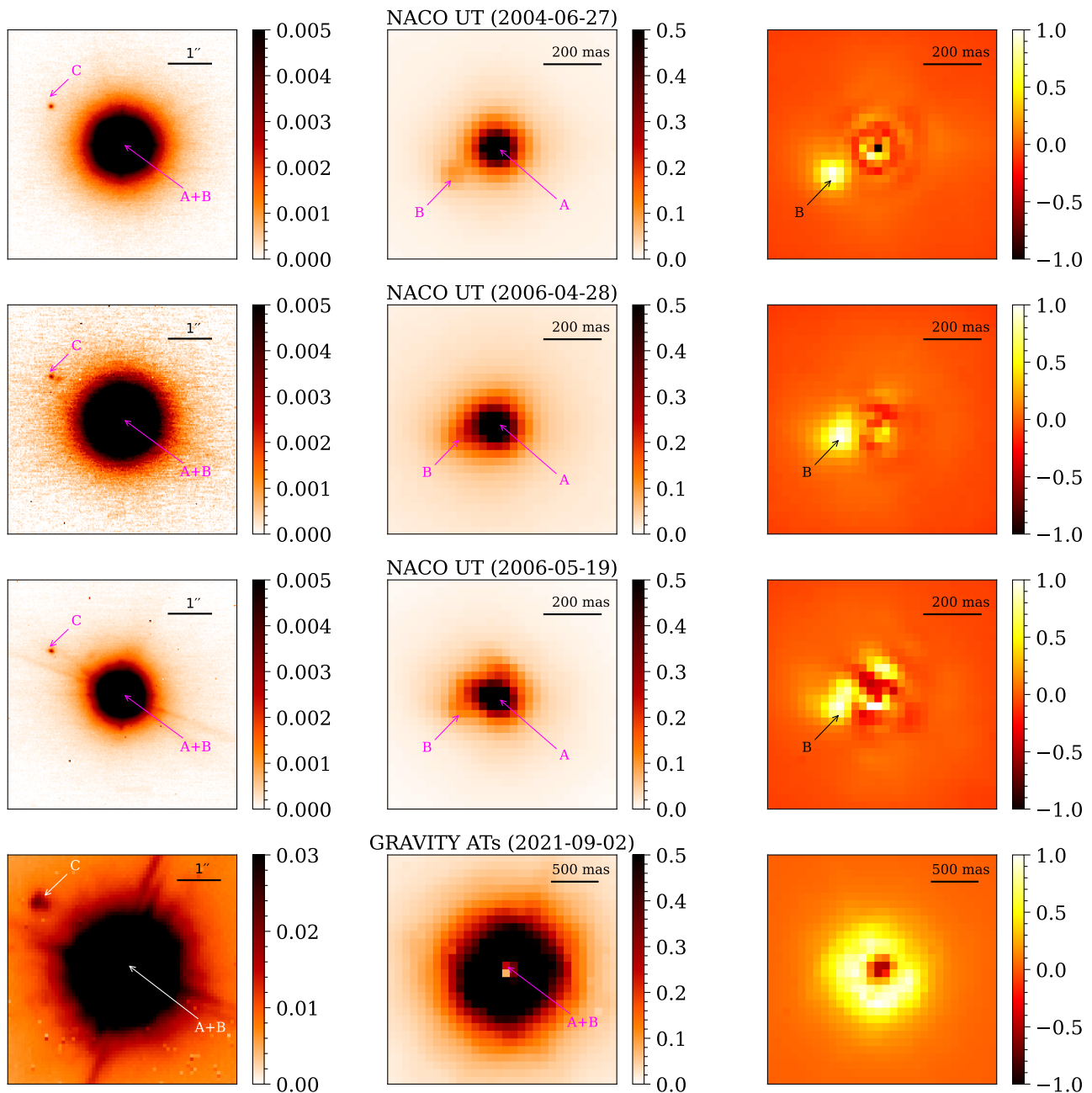


Fig. 3. NIR images of HIP 87813. The first three rows show the NACO observations in K band and the last row shows the image of the acquisition camera of GRAVITY in H band. The left column highlights the faint wide companion (C) reported in De Rosa et al. (2014). The second column highlights the closer companion (B) which we have discovered, while the third column shows the residual image after subtracting the best fit component for the brighter source (A). Note that component B could not be resolved in the GRAVITY image, in which the A component has an effective PSF of FWHM 1'' due to saturation.

high inclination – and therefore could be within the interferometric FOV of PIONIER – does exist, but it will be shown below that that is not the case). On the other hand, the radial velocity variations of the A star suggest a period on the order of days, corresponding to a binary separation on the order of 0.1 AU \leftrightarrow 1.3 mas. Therefore, we expect that the PIONIER observations with an angular resolution of 2.5 mas could be able to spatially resolve component A into a close binary. Indeed, upon inspection the calibrated

interferometric data immediately showed a resolved source with squared visibilities below one and closure phases different than zero. We therefore proceeded to fit the binary model in Eq. 7 to the data, with $f_c = 1$ since it is a very close binary and the fiber attenuation is therefore negligible.

Because our interferometric data consists of squared visibilities and closure phases, the χ^2 map produced by fitting Eqn. 7 to the data is not convex and has many local min-

Table 5. NACO PSF fitting results for deblending of components A and B.

epoch	Δ RA (mas)	Δ DEC (mas)	$\frac{f_B}{f_A}$ %	FWHM _x (mas)	FWHM _y (mas)	θ (deg)	β	χ^2_{red}
2004-06-27	158.5 ± 1.6	-90.7 ± 1.4	6.2 ± 0.2	3.12 ± 0.03	2.94 ± 0.02	0.5 ± 2.4	1.44 ± 0.02	0.82
2006-04-28	124.7 ± 1.6	-35.7 ± 1.4	9.5 ± 0.3	3.46 ± 0.03	3.18 ± 0.03	-4.5 ± 1.9	1.49 ± 0.03	0.18
2006-05-19	133.6 ± 4.0	-23.2 ± 3.2	6.6 ± 0.5	2.77 ± 0.05	3.31 ± 0.06	68.5 ± 1.7	1.33 ± 0.05	5.64

Table 6. Separation between components C and A for the three NACO epochs and C and A+B in the GRAVITY epoch.

epoch	Δ RA (mas)	Δ DEC (mas)
2004-06-27	1656.2 ± 1.1	904.5 ± 1.1
2006-04-28	1638.4 ± 4.6	1026.0 ± 3.3
2006-05-19	1644.3 ± 1.2	1033.0 ± 0.9
2021-09-07 ^a	1628 ± 14	2033 ± 25

Notes.

^(a) Separation between C and A+B because the latter cannot be resolved in the GRAVITY image.

ima. In order to find the global minimum, we run 2d model grids in binary separation for a few different flux ratio to find the approximate region of the global minimum, and proceed with a gradient-based non-linear least squares minimization starting from the best solution in the grid to find the actual global minimum. This is standard practice in fitting a binary model to optical/NIR interferometric data (see e.g. Gallenne et al. 2015). The fits are performed using the `python` package `lmfit`.

With the errorbars reported by the pipeline, the combined reduced χ^2 of the best fit is quite high ($\chi^2_{\text{red}} = 5.8$) and dominated by the squared visibilities; most likely, this is due to systematic errors in the calibration of the squared visibilities. On the other hand, we find very good agreement between data and model for the closure phases (which are more robust to calibration errors). We therefore increased the errors in the visibilities by a factor of 2, which produced a $\chi^2_{\text{red}} = 1.9$ and more balanced residuals between the squared visibilities and closure phases.

Figure 4 shows the PIONIER interferometric data and the best fit binary model, which has a flux ratio $f = 0.10 \pm 0.02$, separation $\rho = 1.7 \pm 0.2$ mas (0.13 ± 0.02 AU) and position angle $\text{PA} = 318.2 \pm 0.9^\circ$. These uncertainties are the 1σ values already scaled by $\sqrt{\chi^2_{\text{red}}}$. From now on, we will refer to the primary star (i.e. the A-type star) in component A as A_1 and the secondary as A_2 .

5. VLTI/GRAVITY

5.1. Acquisition camera image

Although the interferometric GRAVITY data were obtained only for the A star, the acquisition camera of the instrument (which operates in the NIR H band) also shows component C. In Figure 3 we plot the acquisition camera image averaged over the four telescopes in the bottom left. From the image we measured the separation between com-

ponents (A+B) and C, which is reported in Table 6, and a magnitude contrast $\Delta m_H = 7.00 \pm 0.05$.

The module NAOMI provides AO correction which under ideal conditions returns a PSF close to the diffraction limit for the 1.8 m ATs in the H band (FWHM around 250 mas). However, component A is so bright that due to saturation the effective PSF in the acquisition camera image is much broader (FWHM around 1"). In the bottom right panel of Figure 3, we show the residual image after subtracting the best-fit elliptical Moffat profile to the image. Unfortunately, component B cannot be resolved within the residuals of the very broad saturated PSF.

5.2. Interferometric data

The GRAVITY data consists of squared visibilities very close to unity and closure phases very close to zero (i.e. consistent with a single star), and do not immediately reveal the presence of any additional companion. In Fig. 5 we plot the interferometric data (squared visibilities and closure phases) for the SC channel for one of the GRAVITY files. The fact that the very close companion detected in the PIONIER observation is not detected in the GRAVITY data is not surprising due to the lower spatial resolution of the latter. We show in black in Figure 5 the interferometric signatures created by the best-fit binary model to the PIONIER data: clearly, the signatures are too small to be distinguished from a single star model within the errors.

Contrary to the PIONIER data, however, the interferometric FOV of the GRAVITY data is very large (30"), and therefore it is sensitive to wide companions out to a separation of about 300 mas. This separation limit is imposed by the fiber coupling factor: a source located at 150 mas from the center of light will be attenuated by about 50% and one at 300 mas by about 94%. Therefore, it was somewhat of a surprise that the component B seen in the NACO images was not seen in the GRAVITY interferometric data. This implies that the separation between components A and B was larger in the GRAVITY epoch so that the flux from B got significantly attenuated.

5.3. Companion detection limits

We follow Absil et al. (2011) to calculate flux ratio upper limits for a companion as a function of separation. Namely, we first re-scale the error bars so that $\chi^2_{\text{red}} = 1$ for a single star model. Next, we construct a 2D grid in $1 \text{ mas} < \rho < 320 \text{ mas}$ and $0^\circ < \text{PA} < 360^\circ$ and, for each point on the grid, inject an additional source in the model and find the flux ratio at which the model becomes inconsistent with the data at the 3σ level. Due to the sparse

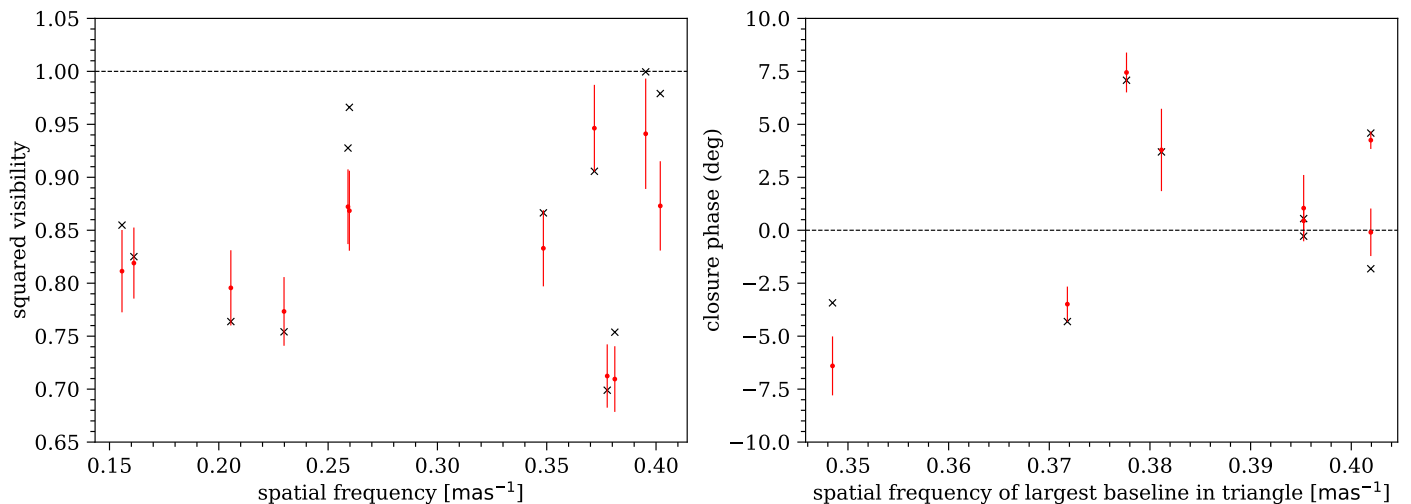


Fig. 4. Data (red) and best fit binary model (black crosses) for the PIONIER observation of HIP87813. The dashed lines show the expected values for a single star, which is clearly ruled out.

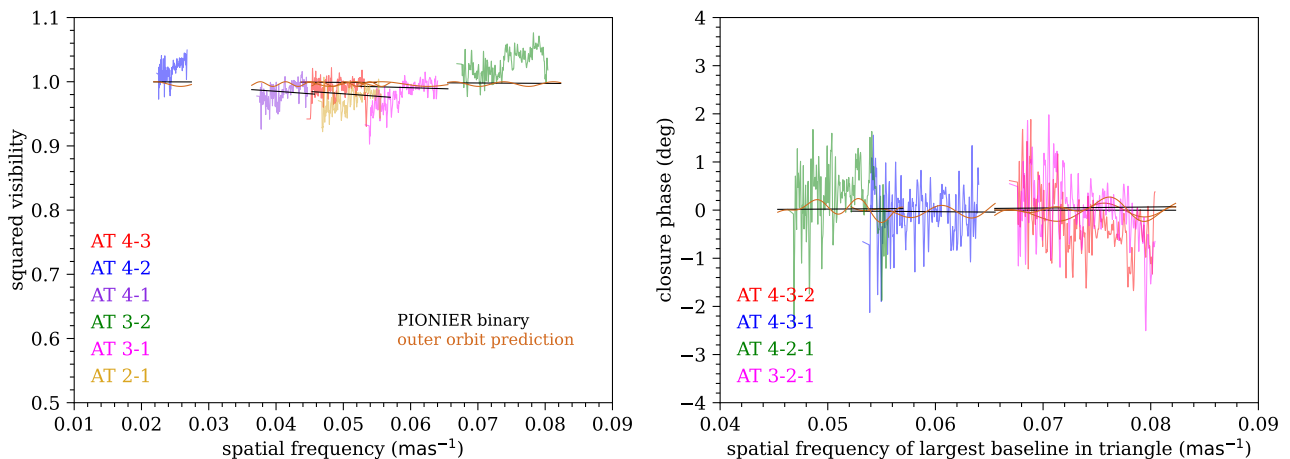


Fig. 5. Science channel interferometric data for the GRAVITY observation of HIP 87813, with each baseline/triangle shown in a different color. The black and orange lines show the interferometric signatures created by the best-fit model for the inner binary A_1+A_2 detected in PIONIER and for the binary $A+B$ predicted from the outer orbit in Section 5.

uv -coverage, the flux ratio upper limit at a given separation depends on the PA (in other words, there are specific positions where the source can be injected and lead to smaller interferometric signatures). Therefore, for each separation we show the median and the 90% flux limits over the full range of PAs. Fig. 6 shows the resulting companion detection limits from the GRAVITY data.

In general, the contrast upper limit degrades at low separations due to the limited angular resolution of the array and at large separations due to the attenuation of the light from the source coupled into the GRAVITY fiber. The results in Fig. 6 corroborate the fact that the companion with flux ratio 10% at separation $\rho = 1.7$ mas detected in the PIONIER observations cannot be seen in the GRAVITY data. It also shows that for component B (detected in NACO images) with a flux ratio 6.2% not to be seen in the GRAVITY data, its separation must be $\rho \gtrsim 200$ mas. Using the 90% completeness curve, the GRAVITY data also allows to exclude any additional companion with a flux ratio $f > 3\%$ within $7 \text{ mas} \lesssim \rho \lesssim 150 \text{ mas}$.

5. Putting it all together: the components of HIP 87813

1. The very faint companion is a background source

We plot the separation between components C and A(+B, in the case of the GRAVITY image) as a function of time in Figure 7. The data is well-fit by a linear motion of $-4.0 \pm 1.9 \text{ mas yr}^{-1}$ in RA and $+67.5 \pm 0.8 \text{ mas yr}^{-1}$ in DEC over 18 years. We note that a small systematic error in the GRAVITY separation is expected due to the fact that components A and B cannot be resolved and due to saturation of the camera.

This motion is quite close to the opposite of the proper motion of HIP 87813 (which we find precisely in Section 5 below). Furthermore, it is not consistent with a Keplerian orbit: the characteristic velocity of the (supposedly) M star around the A+B system would be $v \sim \frac{2\pi 200 \text{ AU}}{1450 \text{ yrs}} \sim 4 \text{ km s}^{-1}$, where an orbit size of $2.6'' \rightarrow 200 \text{ AU}$ and the corresponding period for a total mass $\sim 3.8M_\odot$ were used, which is about a factor of seven smaller than the linear motion measured. Therefore, we conclude with certainty

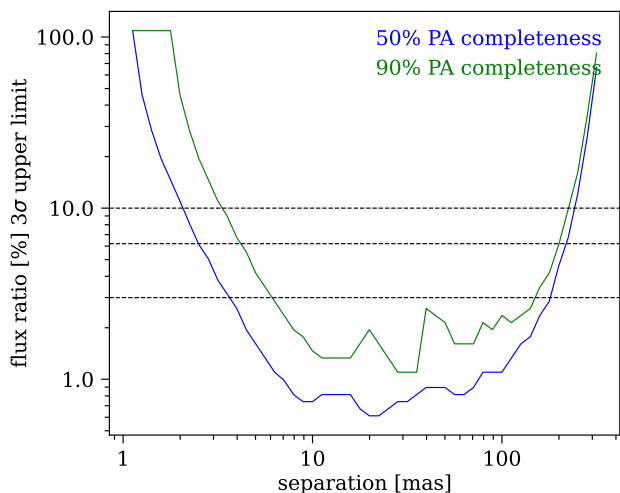


Fig. 6. Companion detection limit for the GRAVITY data as a function of separation. The blue and green curves show the maximum flux ratio allowed for 50% and 90% of the PAs respectively. The horizontal lines demark flux ratio upper limits of 3, 6.2 and 10%.

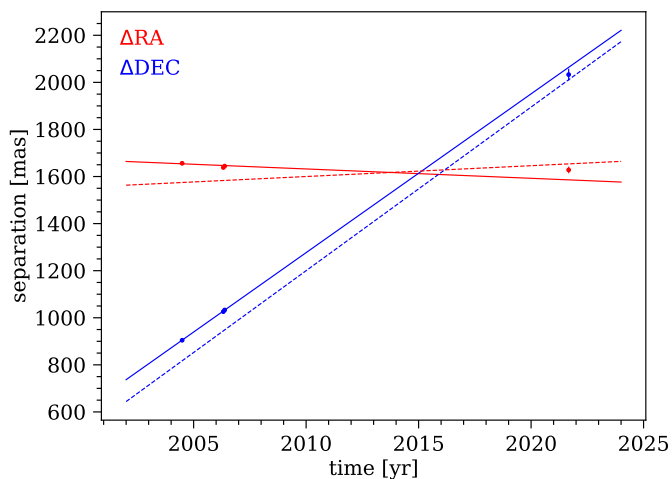


Fig. 7. Separation between components A and C measured from the three NACO images and between A+B and C from the GRAVITY acquisition camera image as a function of time. The full lines show the best-fit linear motion, while the dashed lines show the opposite of the proper motion of HIP 87813 (with an arbitrary vertical shift).

that component C is not physically related to HIP 87813, and is instead a background source with a much smaller proper motion. This is not entirely surprising given that the sky region is quite crowded. Using the 2MASS catalogue (Skrutskie et al. 2006) we calculated that the number density of sources with $K < 13(14)$ within $5'$ of HIP 87813 is $1.7(3.1) \times 10^{-3} \text{ arcsec}^{-2}$, which correspond to a non-negligible number of about 0.02(0.04) background sources in a $2''$ circle around it.

2. The masses of the components

From the data presented above, it is clear that HIP 87813 is a hierarchical triple system consisting of an inner binary (A = $A_1 + A_2$) and an outer tertiary (B). From the PIONIER

data we found $\frac{f_{A_2}}{f_{A_1}} = 0.10 \pm 0.02$ in the H band (the K band flux ratio is the same within the errors; see below) and from the NACO images we found $\frac{f_B}{f_{A_1} + f_{A_2}} = 0.062 \pm 0.002$ in K band. From the total apparent K band magnitude in 2MASS $K = 5.70$ and a distance $d = 78.2 \text{ pc}$, the total absolute magnitude is $K = 1.24$. We can therefore solve for the absolute K band magnitude of each component. We find $K_{A_1} = 1.41 \pm 0.02$, $K_{A_2} = 3.9 \pm 0.2$ and $K_B = 4.33 \pm 0.04$.

For stars with $2.5 \lesssim M_K \lesssim 5.5$ ($0.6M_\odot \lesssim M \lesssim 1.5M_\odot$), there exists a rather tight log-linear K band magnitude-mass relation (e.g. Henry & McCarthy 1993), with small deviations for very young stars (age $\lesssim 100 \text{ Myrs}$). Using Figure A.5 (right) in De Rosa et al. (2014), which was constructed from theoretical isochrones from Baraffe et al. (1998), we find an approximate relation

$$\log M[M_\odot] \approx -0.145M_K + 0.496 \quad (9)$$

Applying this to stars A_2 and B, we find masses $M_{A_2} = 0.85 \pm 0.06$ (G8V-K2V) and $M_B = 0.74 \pm 0.01$ (K3V). Note that the PIONIER flux ratio is in the H band and not in the K band. Approximating star A_1 as a blackbody with $T \sim 9290 \text{ K}$ and star A_2 with $T \sim 5240 \text{ K}$, the ratio between the flux ratio in the H band to that in the K band is 90%. Such a 10% correction is only half of the flux ratio error, and therefore negligible in this case.

For A stars, the age effect is much more important and a precise mass cannot be obtained from the absolute K band magnitude alone. From Figure A.5 (left) in De Rosa et al. (2014), the mass of A_1 for its $M_K = 1.41$ is in the range $1.8 - 2.7M_\odot$ for ages between 63 Myrs and 1 Gyr. Based on the $M_{V_T} - M_K$ color (where V_T is the Tycho visual magnitude) and using theoretical isochrones from Siess et al. (2000) (for solar metallicity and a non-rotating star), De Rosa et al. (2014) estimated a mass $M_{A_1} \sim 2.11M_\odot$ and age $t = 350 \text{ Myrs}$ for the A star. However, the two components A_2 and B make the A star appear redder (and therefore older) than it really is. Using an approximate relation between $M_{V_T} - M_K$ and M_K derived from close main sequence stars with $M_K \sim 4$ in *Gaia*, 2MASS and Tycho:

$$M_{V_T} - M_K \approx 1.3M_K - 2.8 \quad (10)$$

we estimate M_{V_T} for stars A_2 and B, and find the real $M_{V_T} \approx 1.49$ for the A star alone using the total $M_{V_T} = 1.47$ (as expected, the change in M_{V_T} is much smaller than M_K because the contaminants are lower mass stars). Finally, using the corrected $M_K = 1.41$ and $M_{V_T} - M_K = 0.08$ for the A star we find an age $\log(t) \approx 8.25 \Rightarrow t \approx 180 \text{ Myrs}$ using Fig. A.3 in De Rosa et al. (2014), and a corresponding mass $M_{A_1} \approx 2.2M_\odot$ using their Fig. A.4. The isochrones ignore rotation so that, although the A star is not rotating very fast ($v \sin i \approx 60 \text{ km s}^{-1}$), this age estimate should be taken as an upper limit. Furthermore, because this mass estimate is not free of systematic errors, we do not fix the mass of the A star in the further analysis, but a lower limit $M_{A_1} > 1.8M_\odot$ is quite robust.

3. The RV curve of the inner binary

The A star is clearly variable in radial velocity, pointing to a binary system with a period on the order of days. We fit the RV data with a model for a Keplerian orbit:

$$v_{z,1} = -K_1(e \cos(\omega + \pi) + \cos((\omega + \pi) + \nu)) + \gamma \quad (11)$$

where K_1 is the radial velocity semi-amplitude of the primary star (A_1), e is the eccentricity, ω is the argument of periastron, ν is the eccentric anomaly (which involves the other two parameters of the solution, orbital period P_{orb} and time of periastron T_p) and γ is the systemic velocity. Note that we define $\omega = \omega_2$ as the argument of periastron of the secondary star (A_2), so that $\omega_1 = \omega + \pi$. This consistency is important when combining the RV and interferometric data below. The best solution is found assuming Gaussian statistics for the errors through χ^2 minimization using gradient-based nonlinear least squares using the python package `lmfit`. In order to find the global minimum, we perform fits over a finely sampled 2d grid in P_{orb} and e , estimating initial values for the other parameters at each grid point using the data (e.g. Milson et al. 2020). The latter is constraining enough that a clear global minimum exists for the orbital solution. Although the errorbars for the literature and especially for the FEROS RVs are much smaller than the SpeX RVs, the latter have a crucial role in the fit because they provide orbital phase coverage that would otherwise be missing.

Furthermore, we also allowed for an absolute velocity shift between the different data sets (the three Nordstrom & Andersen (1985) points, the Grenier et al. (1999) point, the FEROS points and the SpeX and GRAVITY points) in order to take into account possible systematic errors in the zero points between the different sets, caused for e.g. by instrumental absolute wavelength calibration errors or errors in the effective rest wavelength of the different absorption lines used (intrinsic or due to blending of weaker lines). Shifts could also be caused in the presence of a longer period orbit, since the different data sets are acquired around a decade from each other. The best-fit shifts of the datasets relative to the FEROS dataset are reported in Table 7 and are consistent with or very close to zero.

The reduced χ^2 of the best-fit RV curve is 4.5, which suggests the errorbars may be underestimated by around a factor of two. The best-fit parameters and errors (already scaled by $\sqrt{\chi_{\text{red}}^2}$) are reported in Table 7, and the best fit is shown in Fig. 8 (with the absolute shifts subtracted).

We find that the orbit is moderately eccentric with $e = 0.36 \pm 0.03$ and a period $P = 13.4$ days. The resulting mass function is

$$\frac{M_{A_2}^3}{(M_{A_2} + M_{A_1})^2} (\sin i)^3 = \frac{P_{\text{orb}}}{2\pi G} K_1^3 (1 - e^2)^{3/2} \quad (12)$$

$$= 0.055 \pm 0.016 M_{\odot} \quad (13)$$

Using $M_{A_2} = 0.85 \pm 0.06 M_{\odot}$, the semi-major axis is $a = 0.153 - 0.168$ AU for $M_{A_1} = 1.8 - 2.7$. For the minimum A_1 mass of $1.8 M_{\odot}$, we have $i = 54^\circ \pm 10^\circ$ (or $i = 126^\circ \pm 10^\circ$). For $M_{A_1} = 2.2 M_{\odot}$ as estimated from the theoretical isochrones, we have $i \approx 70^\circ \pm 20^\circ$ or $110^\circ \pm 20^\circ$. The minimum inclination for the binary to be eclipsing is about $i \gtrsim \text{arccot}\left(\frac{R_{A_1} + R_{A_2}}{a}\right) \approx \text{arccot}\left(\frac{1.9R_{\odot} + 0.9R_{\odot}}{0.16 \text{ AU}}\right) \approx 85^\circ$.

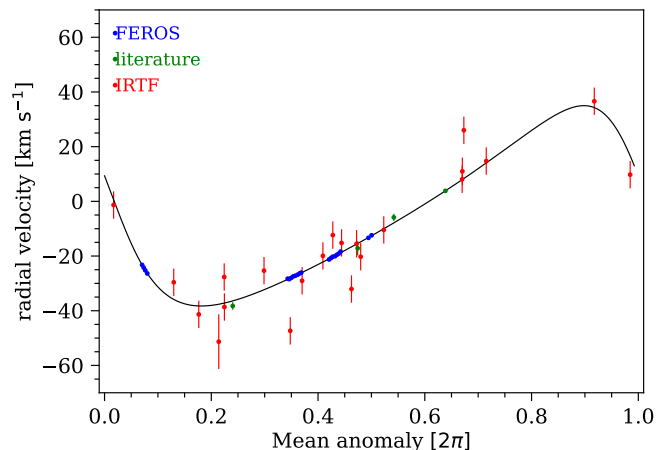


Fig. 8. Data and best-fit radial velocity curve for the orbit of the A-type star A_1 within the close binary A.

While we cannot exclude that $A_1 + A_2$ is an eclipsing binary, it is probably not.

The projected semi-major axis of the A star around the center of mass of the binary

$$a_1 \sin i = K_1 \frac{P}{2\pi} \sqrt{1 - e^2} \approx 0.045 \text{ AU} \leftrightarrow 0.6 \text{ mas} \quad (14)$$

matches the astrometric noise (0.62 mas) of HIP 87813 in *Gaia* eDR3, and is therefore very likely its dominant cause. The size of the semi-major axis on sky is $a \approx 0.16$ AU \leftrightarrow 2 mas and can be readily identified with the binary resolved by PIONIER.

4. The orientation of the inner binary

Although a single astrometric point is not enough to completely determine the remaining two Keplerian parameters of the $A_1 + A_2$ orbit (i.e. the inclination i and the longitude of the ascending node Ω), it can be used to significantly constrain them (and therefore the 3d orientation of the binary). We do this by building a grid in $i \in [0^\circ, 180^\circ]$ and $\Omega \in [0^\circ, 360^\circ]$ and finding the difference between the predicted (from the Keplerian orbit) and the measured $\Delta\text{RA} = -1.13 \pm 0.13$ mas and $\Delta\text{DEC} = 1.27 \pm 0.15$ mas in the PIONIER observation. The remaining orbital parameters are taken from the best-fit model to the RV curve, and $M_{A_2} = 0.85 M_{\odot}$ is also used (so that M_{A_1} is calculated from the mass function and the inclination). We note that the resulting uncertainty in i and Ω is much larger than for the other orbital parameters determined from the RV curve, so that fixing the latter to their best-fit values (rather than performing a joint fit) is appropriate.

In Figure 9 (left) we plot the resulting averaged (over ΔRA and ΔDEC) squared residual χ_{avg}^2 . The green lines mark the $\chi_{\text{avg}}^2 = 1, 2, 3, 4$ and 5 contours. There is clearly a large correlation between i and Ω , and Ω is particularly well-constrained. Taking the $\chi_{\text{avg}}^2 = 2$ contour, for example, the allowed range is $35^\circ \lesssim i \lesssim 145^\circ$ and $120^\circ \lesssim \Omega \lesssim 160^\circ$. The vertical blue lines mark the (1σ) inclination range allowed for a minimum A star mass of $1.8 M_{\odot}$, while the

Table 7. Best-fit radial velocity curve parameters for the A₁+A₂ binary.

K_1	$36.6 \pm 3.4 \text{ km s}^{-1}$
e	0.36 ± 0.03
P_{orb}	$13.4193 \pm 0.0006 \text{ days}$
ω	$72.6 \pm 5.5^\circ$
T_p	$\text{JD } 2457900.1 \pm 0.2$
γ	$-5.6 \pm 1.7 \text{ km s}^{-1}$
Δ_{vz} Nordstrom & Andersen (1985)	$-3.8 \pm 3.5 \text{ km s}^{-1}$
Δ_{vz} Grenier et al. (1999)	$0.1 \pm 2.0 \text{ km s}^{-1}$
Δ_{vz} SpeX/GRAVITY	$-5.5 \pm 2.6 \text{ km s}^{-1}$

Notes.

vertical cyan lines mark the inclination (plus 1σ ranges) for $M_{A_1} = 2.2M_\odot$ as estimated from the theoretical isochrones.

In Figure 9 (right), we plot a few projected orbits for which $\chi_{\text{avg}}^2 < 1$, with the PIONIER measurement in black and the primary star A₁ at the origin, in order to illustrate the procedure. The inclinations vary from 50° to 130° in rainbow order. In the near future, either more interferometric observations or the *Gaia* DR3 release will probably fully determine the orbit.

5. The orbit of the outer binary

In this section, we constrain the parameters of the outer orbit between A=A₁+A₂ and B, establishing HIP 87813 as a hierarchical triple system. We do this by combining the separations measured in the three NACO images with the proper motions listed in Table 1 (except for the FOCAT-S point since we do not know how apart the epochs used to derive the proper motion are separated) and the positions listed in Table A.4. For the latter, besides *Hipparcos* and *Gaia*, we also use a position from the Guide Star Catalog (GSC) version 2.3.2 (Lasker et al. 2008) with 10 mas error. We take the *Hipparcos* position as the reference position (only positional differences matter for the fit). The parameters consist of six orbital parameters, the mass of star A₁ and the two intrinsic linear proper motions in RA and DEC. Combining all the data, there are 12 measurements for the positions (RA and DEC), 8 measurements for the proper motions and 3 measurements for the direct separation.

Because *Hipparcos*, *Gaia* and GSC do not resolve components A and B, they measure the motion of the center of light (COL) around the center of mass (COM). It traces the same Keplerian motion as the primary star but with a semi-major axis somewhat reduced. The semi-major axis of the COL relative to the COM is

$$a_{\text{COL}} = \left| \frac{-f_A a_A + f_B a_B}{f_A + f_B} \right| = a_A \frac{1-f}{1+f} \quad (15)$$

where $f = \frac{f_B}{f_A}$ is the flux ratio and $q = \frac{M_B}{M_A}$ is the mass ratio between the components. For identical stars, there is

Table 8. Best-fit parameters for the outer orbit A+B.

e	0.26 ± 0.03
i	$71.6^\circ \pm 3.2^\circ$
ω	$160.5^\circ \pm 19.6^\circ$
Ω	$130.1^\circ \pm 5.5^\circ$
P_{orb}	$60.8 \pm 12.0 \text{ yrs}$
T_p	1997.2 ± 2.1
M_{A_1}	$1.61 \pm 0.51 M_\odot$
pmra	$-4.6 \pm 0.4 \text{ mas yr}^{-1}$
pmdec	$-69.5 \pm 0.9 \text{ mas yr}^{-1}$

no astrometric motion. In our case, with $f = 0.062$ and $q \sim 0.25$, we expect the COL to follow the primary "star" (A=A₁+A₂) with about a 20% reduction in semi-major axis.

We fit for the Keplerian orbit that can best explain all the data. We use linear least squares implemented with the python package `lmfit` and run fits over a fine eccentricity grid between 0.01 and 0.99 (we find that keeping the eccentricity fixed helps to prevent the fit from diverging). We find a well-defined global minimum with $\chi_{\text{red}}^2 = 4.55$ and its parameters and errors (scaled by $\sqrt{\chi_{\text{red}}^2}$) are reported in Table 8. We find the outer orbit to be mildly eccentric ($e = 0.26 \pm 0.03$) with a period $P_{\text{orb}} = 60.8 \pm 12.0 \text{ yrs}$. We also note that the mass of the A star, which was let free to vary, has a best fit value $M_{A_1} = 1.61 \pm 0.51 M_\odot$, consistent with the allowed range $M_{A_1} > 1.8 M_\odot$ but too uncertain for a useful constraint. The resulting semi-major axis of the outer orbit is $a \approx 24 \text{ AU}$.

In Figure 10, we plot the data and the best fit for the outer orbit. The upper left panel shows the separation from the NACO images, the bottom left panel shows the tangential velocities (already with the best-fit proper motion

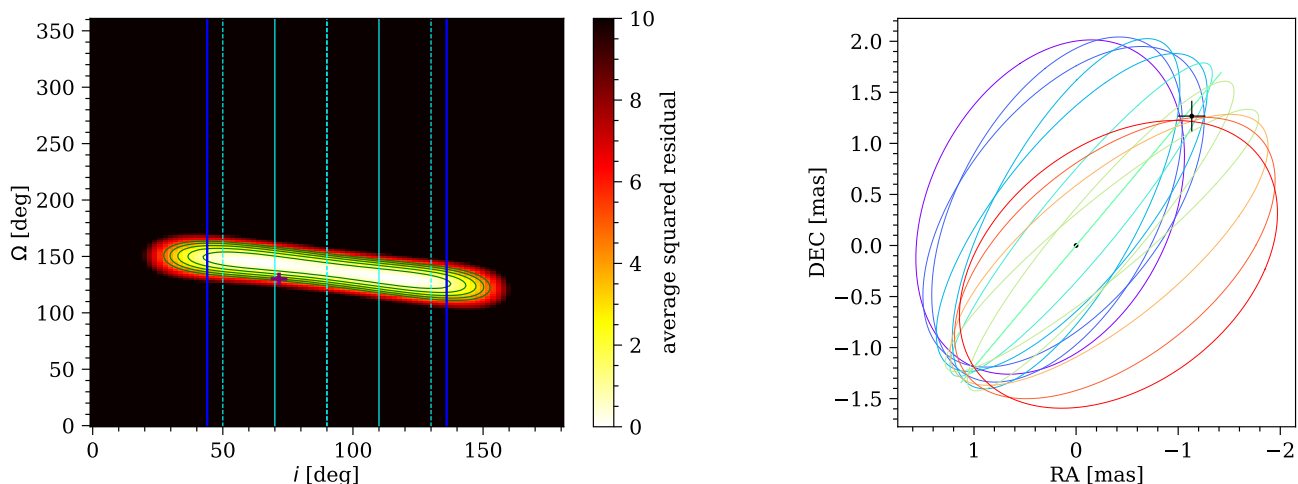


Fig. 9. **Left:** Average squared residual for the on-sky separation of the A_1+A_2 binary in the PIONIER observation as a function of the inclination and longitude of the ascending node. The green lines mark the 1, 2, 3, 4 and 5 contours (for the blue vertical lines see text). The magenta point marks the orientation of the outer orbit A+B. **Right:** Locus of a few possible projected binary orbits that give an average squared residual to the PIONIER point (black) less than one, for inclinations varying from 50° to 130° in rainbow order. The primary star A_1 is at (0,0).

subtracted) and the bottom right panel shows the positions (relative to the *Hipparchos* position and also subtracted for the best-fit proper motion), with the FOCAT-S points (not used in the fit) marked with "x". In the upper right panel, we show the velocity shifts measured from the RV curve (relative to the FEROS dataset in 2005) compared to the model. While we decided to not use these data in the fit for the reasons discussed in Section 3, they are consistent with the model (within their large errors relative to the orbital motion).

Finally, we calculate the predicted separation between components A and B at the time of the PIONIER and GRAVITY interferometric observations, shown as the vertical green lines in the upper right panel of Figure 10. The predicted separation at the PIONIER epoch is 150 mas, so component B was indeed well outside the interferometric FOV and invisible to PIONIER. Meanwhile, the predicted separation at the GRAVITY epoch is 282 mas. We plot the interferometric signature that the B component at this separation would create in the GRAVITY data in Figure 5. Indeed, the increase in separation explains why B could not be detected in the GRAVITY data.

6. The relative orientation between the inner and outer orbits

In Figure 9 (left), we plot in magenta the orientation of the outer orbit measured in the previous section. Remarkably, it falls within the constraints of the orientation of the inner binary, and is consistent with the $\chi_{\text{avg}}^2 = 2$ surface within 1σ . It also falls very close to the inclination needed to make $M_{A_1} = 2.2M_\odot$ as estimated from theoretical isochrones. This is strong albeit not definitive evidence that the inner and outer orbits are coplanar.

In order to quantify this, we compute the volume of the sphere contained within the $\chi_{\text{avg}}^2 = 2$ contour of the inner orbit orientation and find 4%. While there remain allowed regions for which the relative inclination is larger than 40° (for e.g. if $i_{\text{inner}} \sim 110^\circ$ and the orbits are “mirrored”), we argue that the data is suggestive of coplanarity. A definitive

answer should soon be reached once the orientation of the inner binary is more tightly constrained.

6. Discussion

We have shown that HIP 87813=HJ 2814A is a hierarchical triple. The inner binary (A= A_1+A_2) consists of a $\sim 2.2M_\odot$ A-type star and a $0.85M_\odot$ star on a very close ($a = 0.16$ AU, $P = 13.4$ days) and mildly eccentric ($e = 0.36$) orbit. The outer companion (B) is a $0.74M_\odot$ star on a $P \sim 60$ yrs ($a \sim 24$ AU), also mildly eccentric ($e = 0.26$) orbit. The system also orbits another solar-mass 2 AU binary, HJ 2814B (D= D_1+D_2), over a period $P \sim 26$ kyrs ($a \sim 1600$ AU). Finally, the faint star 2" away from HIP 87813 reported in De Rosa et al. (2014) turned out to be a background source. A schematic summary of the system is shown in Figure 1. The quintuple HJ2814 therefore joins a small list of high multiplicity systems containing an intermediate mass (A type) primary (e.g. Tokovinin 1997; Eggleton & Tokovinin 2008; Tokovinin 2014, 2018).

This system is particularly interesting as it shows separations on three different length scales (triple hierarchy) and involves 5 stars that are sufficiently massive to evolve into WDs on the scale of a Hubble time. It is interesting to compare it with some other 5+ multiples with A star primaries known. In the VAST survey (De Rosa et al. 2014), limited to $d \lesssim 75$ pc, there are only two quintuples reported (and no 6+ systems), HIP 11569 and HIP 90156 (both in the North and therefore not part of our VLTI survey). HIP 11569 (45 pc) contains one A star and four $\sim 1M_\odot$ stars, but does not have a very close binary like HIP 87813 (the shortest period is 48.7 yrs). HIP 90156 (58 pc) has one A star and 2 $\sim 1M_\odot$ stars but its quintuple status is not confirmed (it is currently listed as a quadruple in the Updated Multiple Star Catalog; Tokovinin 2018). It is important to notice that the common proper motion search in De Rosa et al. (2014) has been superseded by *Gaia*, and as a result many systems in the VAST survey have had their multiplicity

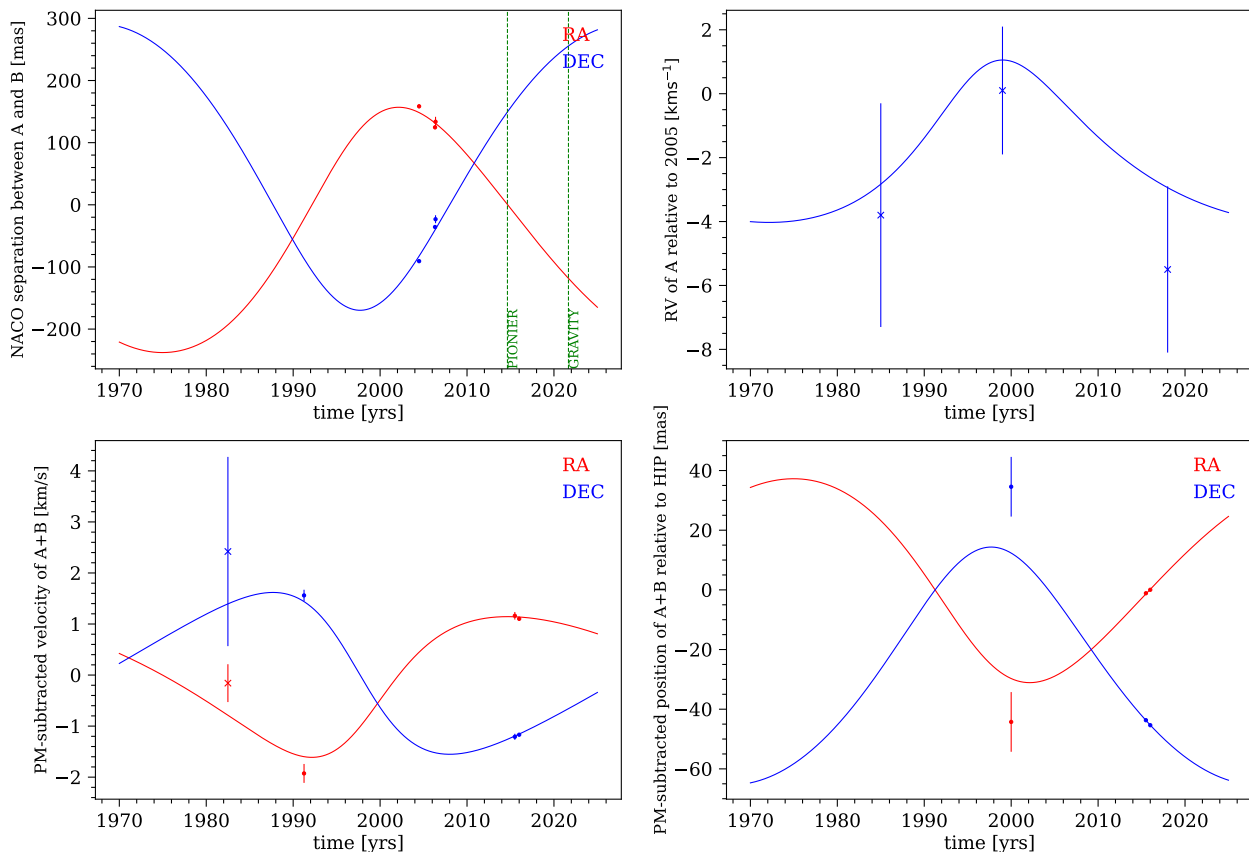


Fig. 10. Data and best fit model for the outer orbit of component $A=A_1+A_2$ around B. **Upper left:** direct separation measured from NACO images. The vertical green lines mark the epochs of NIR interferometric PIONIER and GRAVITY observations. **Lower left:** tangential velocities (proper motion subtracted). **Lower right:** positions relative to *Hipparcos* (proper motion subtracted). **Upper right:** radial velocity relative to 2005 (the FEROS epoch), which were not used for the fit.

ity upgraded with very wide companions in the Updated Multiple Star Catalog.

Therefore, we also searched the latter for 5+ systems with A star primaries and found 2 septuples, 3 sextuples and about 10 quintuples that are at least reasonably well characterized. The majority is located within 200 pc of the Sun but three of them are beyond it. Their properties are varied but many of them show a large number of A or $\sim 1M_\odot$ stars within a triple hierarchy structure (periods of a few to tens of days, decades to centuries, and few to tens of kyrs), for e.g. HIP 36850, HIP 21402, HIP 56109 and HIP 41564 within 100 pc, and HIP 107162 and HIP 58112 beyond it. Therefore, while HJ 2814 is rare it is certainly not unique, and these systems may share a common origin or fate. As far as we can tell none of these systems have been observed with interferometry, so that the strength of Kozai-Lidov oscillations within the inner hierarchy (see below) is not constrained. Quantitative estimates of the abundance and statistical properties of similar systems are needed to make progress but are beyond the scope of this paper.

1. Dynamical processes in the quintuple system

The constraints on the configuration obtained from the observations described above allow us to narrow down the dynamical behaviour of this system.

The high hierarchy implies that the system is dynamically stable. Over short time scales, the 5 stars will move along the 4 Keplerian orbits involved (A1-A2, A-B, D1-D2, AB-D). Over long time scales, hierarchical systems can exchange significant angular momentum leading to precession and oscillations in eccentricity and inclination of the inner orbits (Kozai-Lidov oscillations Lidov (1962); Kozai (1962), see Naoz (2016); Ito & Ohtsuka (2019) for recent reviews). In particular, excitation of the eccentricity by a third object has been argued to lead to orbital shrinkage due to tidal dissipation (e.g. Kiseleva et al. 1998; Fabrycky & Tremaine 2007; Naoz & Fabrycky 2014) and it is natural to ask if the close binary A1-A2 is currently experiencing such a process. The Kozai-Lidov oscillation time of the A1-A2 + B triple system is roughly given by $\tau_{KL} \sim P_{\text{out}}^2/P_{\text{in}} \sim 10^5$ years, where $P_{\text{out}} = 60$ years is the outer A-B orbital time and $P_{\text{in}} = 13.4$ days is the inner A1-A2 orbital time, and is certainly short enough. In order that eccentricity changes significantly, the mutual inclination has to be sufficiently high and the oscillations need to be faster than the General Relativistic (GR) precession time. For the masses and separation scales of this triple system, a hierarchy $a_{\text{out}}/a_{\text{in}}$ smaller than ~ 100 is required to overcome GR precession (using Eq. 5 in Dong et al. 2014, with low outer eccentricity). The measured hierarchy of $24\text{AU}/0.16\text{AU}=150$ is marginal implying that oscillations may be possible de-

pending on the mutual inclination and requiring a detailed determination of the orbital parameters. Despite the significant degeneracy in the orientation of the A1-A2 orbit (Figure 9) a tight constraint on the eccentricity oscillations can be obtained as shown in Figure 11 and described next.

For each choice of orientation of the A1-A2 orbital plane ($i_{\text{in}}, \Omega_{\text{in}}$), the parameters of the triple system A1-A2+B are completely set and the maximal eccentricity that can be achieved in the Kozai-Lidov oscillation can be algebraically found in the quadruple approximation (which is excellent given the high hierarchy). This is obtained by requiring that the sum of the Quadruple and GR Hamiltonians is conserved (e.g. Eqs. 12,22 in Fabrycky & Tremaine 2007), as well as the outer eccentricity (Lidov & Ziglin 1976) and the total angular momentum, and finding the maximal eccentricity among the extrema at $\omega_{\text{in}} = \pi/2$. As can be seen in figure 11, the oscillations obtained within the allowed orientations are negligible. At the present eccentricity, it is likely that the A1-A2 system is experiencing negligible tidal dissipation within a timescale of the age of the system (~ 200 Myr): tidal dissipation in A2 is unlikely as the circularization period of the larger sun-like stars over billions of years is likely shorter than 13 days (e.g. Zahn 1977; Duquennoy & Mayor 1991; Mathieu et al. 2004; Raghavan et al. 2010; Zanazzi 2021) and is a strong function of the period and radius of the star; tidal migration due to dissipation in the primary A1 A-star is largely ruled out by its fast rotation ($v_{\text{rot}} \sin i = 52 \text{ km s}^{-1}$) with a rotation period $p \lesssim 2$ days which is much shorter than the synchronization period (and the pseudo-synchronization period; Hut 1982) - if tidal dissipation was significant, synchronization would have been achieved on much shorter time scales than circularization. The low tidal dissipation in the A-star and lack of synchronization is compatible with estimates for the parameters of the system for a radiative envelope (Zahn 1977).

The behaviour of the A1-A2+B system may be significantly affected by the D system if the pericenter of the AB-D orbit brings it sufficiently close. The only information is the instantaneous projected distance of about 1600 AU which constrains the semi-major axis but provides no information on the eccentricity. At high eccentricity, the Kozai-Lidov time is shortened by a factor of order $(1 - e^2)^{3/2}$. For a semi-major axis of 1600 AU and a high eccentricity $1 - e^2 \lesssim 0.1$ the Kozai-Lidov time scale for precession and oscillations of the AB orbit is reduced to values comparable to that of the A1-A2 orbit enabling changes in the mutual inclination of the A1-A2+B triple system as well as possible changes in the eccentricity of the AB orbit (Hamers et al. 2015) which could then change the conclusion about the possible eccentricity variations of the A1-A2 system. The chance for such a high eccentricity in the AB-D orbit could be substantial. For example, if randomly chosen from a random thermal distribution $dn/de \propto e$, which is likely characteristic of binaries at ~ 1000 AU separations (e.g. Duquennoy & Mayor 1991; Hwang et al. 2022; Tokovinin 2020), the chance for $1 - e^2 < 0.1$ is about 10%. A higher eccentricity $1 - e^2 < 0.05$, (a 5% chance for a thermal distribution), would bring the D system to within 40 AU of the triple which is sufficiently close to allow energy exchange and stochastic semi-major axis evolution of the AB-D orbit over long times (e.g. Heggie 1975; Roy & Haddow 2003; Mushkin & Katz 2020). Without additional information it is thus not possible to determine the dynamical evolution of the system. An accurate determination of the relative

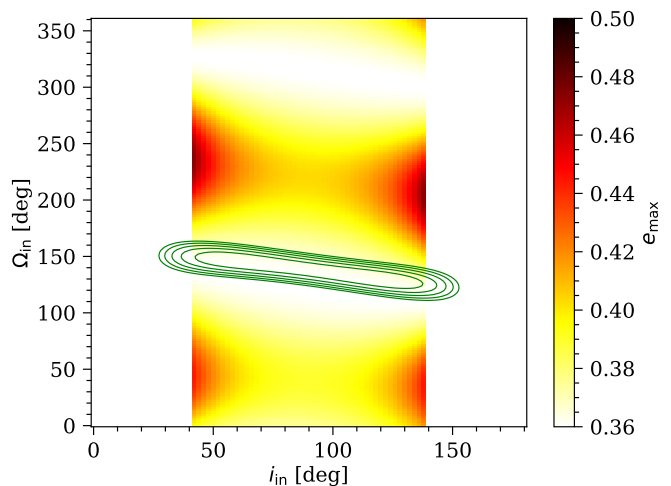


Fig. 11. The maximum eccentricity attainable in A_1+A_2 through Kozai-Lidov oscillations induced by B (under the quadrupolar, averaged approximation). The green contours show the $1-5\sigma$ constraints on the inner orbit, and inclinations for which $M_{A_1} < 1.8M_{\odot}$ have been excluded.

proper motion of the AB-D system, which will hopefully be achieved by future observations (in particular future Gaia releases) may allow useful constraints.

2. X-ray emission

HIP 87813 was detected as an X-ray source by ROSAT in the catalogue of pointed observations with the High Resolution Imager (HRI; ROSAT Scientific Team 2000) in an observation between 1994-09-16 and 26. The count rate of 0.0178 ± 0.0026 photons s^{-1} within 0.1 – 2.4 keV was converted to an X-ray luminosity $L_X \sim 0.95 \times 10^{30}$ erg s^{-1} in the catalogue of X-ray emitting A stars of Schröder & Schmitt (2007). By comparing the reported count rate and X-ray luminosity to other stars at various distances, we noticed that the reported X-ray luminosity for HIP 87813 is exactly a factor of 10 higher than what it should be (most likely due to a typo), so that its actual X-ray luminosity is 10^{29} erg s^{-1} .

Because of the positional error of 1.9" on the X-ray source, we cannot absolutely exclude that X-ray emission is due to the faint background source of unknown nature. However, assuming that the X-ray emission is from HIP 87813, it is mostly probably associated with one or both the late type stars because A stars have neither a convective envelope nor a strong wind (and are therefore the most X-ray inactive class of MS stars). An X-ray luminosity of 10^{29} erg s^{-1} is fully compatible with that expected from early-mid K stars with an age of about 200 Myrs (Garcés et al. 2011), and a rotation period on the order of 10 days (Pizzolato et al. 2003).

3. How did HJ2814 form and how will it evolve?

A study of the formation and future evolution of this systems is beyond the scope of this paper. Below we briefly outline several interesting possibilities which we cannot rule out at this point.

The triple A1-A2+B and the binary D1-D2, which are separated by around 1600 AU, may have formed at that separation (e.g. Pineda et al. 2015; Tokovinin 2017). Alternatively, the entire system formed at a scale of ~ 100 AU, and the D1-D2 binary dynamically migrated outwards due to the multi body gravitational interactions (e.g. Reipurth & Mikkola 2012; Mushkin & Katz 2020). The A-B system is separated by 24 AU, and therefore could have formed by disk fragmentation. The small separation of the inner A1-A2 binary (0.16 AU) is well below the 10 AU limit above which binaries are believed to form *in situ* (e.g. Bate 2009) and suggests that it formed at a larger separation. Inward migration may have occurred due to interactions with the disk (e.g. Artymowicz et al. 1991) or through tidal dissipation enhanced by Kozai-Lidov oscillations (e.g. Kiseleva et al. 1998; Fabrycky & Tremaine 2007; Naoz & Fabrycky 2014). As discussed above, tidal dissipation is unlikely to play a role unless the the AB-D orbit has a high eccentricity with a sufficiently small pericenter, allowing the D1-D2 binary to perturb the A1-A2+B triple. A high eccentricity is expected if the D1-D2 migrated to its large separation due to energy exchanges with the triple. Hence the questions of origin of the large AB-D separation and of the tight A1-A2 are related.

All 5 stars are massive enough to evolve off the main sequence within about a Hubble time. Given the uncertainty in the dynamical effects of the other stars in the system, various outcomes may result for the close binary - a single WD (involving a merger before, during or after the evolution of the A-star), a close MS-WD binary, a close double WD (involving mass transfer that will shorten the MS lifetime of A₂), or even a thermonuclear explosion due to the merger or collision of the possible two WDs. Non trivial evolution is all but guaranteed given that even if nothing else is changed, the A star will expand and fill its Roche lobe reaching a radius of about $15R_{\odot}$ leading to mass transfer.

An important question is to what extent the system will remain bound following the stellar evolution of the A1-A2 system given the expected mass loss when forming the WD/s. There is evidence that WDs obtain natal kicks when forming which are not larger than 1 km/s (El-Badry & Rix 2018) which may unbind the HJ2814A-HJ2814B system but not the HJ2814A system itself. However, given the likely asymmetric mass-loss associated with the A1-A2 binary evolution, larger kicks cannot be ruled out. It is therefore possible that the resulting system will remain in a binary or quintuple system. Given that the stars of HJ2814B can evolve off the main sequence within a Hubble time, an end state with four or five WDs in the same system is possible. Whatever the consequence of such evolution is, similar evolved systems likely exist within the vicinity of the sun and motivates the challenging study of multiplicity of nearby WDs. The complex case of HJ2814 helps to demonstrate the remaining observational challenge as well as the rapidly growing set of observational and theoretical tools in the ongoing study of multiplicity of stars.

Acknowledgements. This work has made use of data from the European Space Agency (ESA) mission Gaia (<https://www.cosmos.esa.int/gaia>), processed by the Gaia Data Processing and Analysis Consortium (DPAC, <https://www.cosmos.esa.int/web/gaia/dpac/consortium>). Funding for the DPAC has been provided by national institutions, in particular the institutions participating in the Gaia Multilateral Agreement. This publication makes use of data products from the Two Micron All Sky Survey, which is a joint project of the

University of Massachusetts and the Infrared Processing and Analysis Center/California Institute of Technology, funded by the National Aeronautics and Space Administration and the National Science Foundation. This research has made use of the Jean-Marie Mariotti Center SearchCal service ³ co-developed by LAGRANGE and IPAG. This research has made use of the CDS Astronomical Databases SIMBAD and VIZIER ⁴, NASA's Astrophysics Data System Bibliographic Services, NumPy (Van Der Walt et al. 2011) and matplotlib, a Python library for publication quality graphics (Hunter 2007).

References

- Abil, O., Le Bouquin, J. B., Berger, J. P., et al. 2011, A&A, 535, A68
 Artymowicz, P., Clarke, C. J., Lubow, S. H., & Pringle, J. E. 1991, ApJ, 370, L35
 Bailer-Jones, C. A. L., Rybizki, J., Fouesneau, M., Demleitner, M., & Andrae, R. 2021, AJ, 161, 147
 Baraffe, I., Chabrier, G., Allard, F., & Hauschildt, P. H. 1998, A&A, 337, 403
 Bate, M. R. 2009, MNRAS, 392, 1363
 Belokurov, V., Penoyre, Z., Oh, S., et al. 2020, MNRAS, 496, 1922
 Bourges, L., Mella, G., Lafrasse, S., et al. 2017, VizieR Online Data Catalog, II/346
 Brandt, T. D. 2018, ApJS, 239, 31
 Brandt, T. D. 2021, ApJS, 254, 42
 Bystrov, N. F., Polojentsev, D. D., Potter, H. I., et al. 1994, Bulletin d'Information du Centre de Données Stellaires, 44, 3
 Cushing, M. C., Vacca, W. D., & Rayner, J. T. 2004, PASP, 116, 362
 De Rosa, R. J., Patience, J., Wilson, P. A., et al. 2014, MNRAS, 437, 1216
 Dong, S., Katz, B., & Socrates, A. 2014, ApJ, 781, L5
 Duchêne, G. & Kraus, A. 2013, ARA&A, 51, 269
 Duquenois, A. & Mayor, M. 1991, A&A, 248, 485
 Eggleton, P. P. & Tokovinin, A. A. 2008, MNRAS, 389, 869
 El-Badry, K. & Rix, H.-W. 2018, MNRAS, 480, 4884
 Fabrycky, D. & Tremaine, S. 2007, ApJ, 669, 1298
 Gaia Collaboration, Brown, A. G. A., Vallenari, A., et al. 2018, A&A, 616, A1
 Gaia Collaboration, Brown, A. G. A., Vallenari, A., et al. 2021, A&A, 649, A1
 Gallenne, A., Mérand, A., Kervella, P., et al. 2015, A&A, 579, A68
 Gao, Y., Toonen, S., & Leigh, N. 2022, arXiv e-prints, arXiv:2203.05357
 Garcés, A., Catalán, S., & Ribas, I. 2011, A&A, 531, A7
 Glebocki, R. & Gnacinski, P. 2005, VizieR Online Data Catalog, III/244
 Gravity Collaboration, Abuter, R., Accardo, M., et al. 2017, A&A, 602, A94
 Grenier, S., Burnage, R., Faraggiana, R., et al. 1999, A&AS, 135, 503
 Hamers, A. S., Perets, H. B., Antonini, F., & Portegies Zwart, S. F. 2015, MNRAS, 449, 4221
 Hamers, A. S., Rantala, A., Neunteufel, P., Preece, H., & Vynatheya, P. 2021, MNRAS, 502, 4479
 Harrington, R. S. 1968, AJ, 73, 190
 Heggie, D. C. 1975, MNRAS, 173, 729
 Henry, T. J. & McCarthy, Donald W., J. 1993, AJ, 106, 773
 Hillebrandt, W. & Niemeyer, J. C. 2000, ARA&A, 38, 191
 Hunter, J. D. 2007, Computing In Science & Engineering, 9, 90
 Hut, P. 1982, A&A, 110, 37
 Hwang, H.-C., Ting, Y.-S., & Zakamska, N. L. 2022, MNRAS, 512, 3383
 Ito, T. & Ohtsuka, K. 2019, Monographs on Environment, Earth and Planets, 7, 1
 Katz, B. & Dong, S. 2012, arXiv e-prints, arXiv:1211.4584
 Kaufer, A., Stahl, O., Tubbesing, S., et al. 1999, The Messenger, 95, 8
 Kiseleva, L. G., Eggleton, P. P., & Mikkola, S. 1998, MNRAS, 300, 292
 Klein, Y. Y. & Katz, B. 2017, MNRAS, 465, L44
 Kozai, Y. 1962, AJ, 67, 591
 Kushnir, D., Katz, B., Dong, S., Livne, E., & Fernández, R. 2013, ApJ, 778, L37

³ Available at <http://www.jmmc.fr/searchcal>

⁴ Available at <http://cdsweb.u-strasbg.fr/>

- Lapeyriere, V., Kervella, P., Lacour, S., et al. 2014, in Society of Photo-Optical Instrumentation Engineers (SPIE) Conference Series, Vol. 9146, Optical and Infrared Interferometry IV, ed. J. K. Rajagopal, M. J. Creech-Eakman, & F. Malbet, 91462D
- Lasker, B. M., Lattanzi, M. G., McLean, B. J., et al. 2008, *AJ*, 136, 735
- Le Bouquin, J. B., Berger, J. P., Lazareff, B., et al. 2011, *A&A*, 535, A67
- Lenzen, R., Hartung, M., Brandner, W., et al. 2003, in Society of Photo-Optical Instrumentation Engineers (SPIE) Conference Series, Vol. 4841, Instrument Design and Performance for Optical/Infrared Ground-based Telescopes, ed. M. Iye & A. F. M. Moorwood, 944–952
- Lidov, M. L. 1962, *Planet. Space Sci.*, 9, 719
- Lidov, M. L. & Ziglin, S. L. 1976, *Celestial Mechanics*, 13, 471
- Lindegren, L., Klioner, S. A., Hernández, J., et al. 2021, *A&A*, 649, A2
- Maoz, D., Mannucci, F., & Nelemans, G. 2014, *ARA&A*, 52, 107
- Mathieu, R. D., Meibom, S., & Dolan, C. J. 2004, *ApJ*, 602, L121
- Milson, N., Barton, C., & Bennett, P. D. 2020, arXiv e-prints, arXiv:2011.13914
- Moe, M. & Di Stefano, R. 2017, *ApJS*, 230, 15
- Moffat, A. F. J. 1969, *A&A*, 3, 455
- Murphy, S. J., Moe, M., Kurtz, D. W., et al. 2018, *MNRAS*, 474, 4322
- Mushkin, J. & Katz, B. 2020, *MNRAS*, 498, 665
- Naoz, S. 2016, *ARA&A*, 54, 441
- Naoz, S. & Fabrycky, D. C. 2014, *ApJ*, 793, 137
- Nordstrom, B. & Andersen, J. 1985, *A&AS*, 61, 53
- Perets, H. B. & Fabrycky, D. C. 2009, *ApJ*, 697, 1048
- Pineda, J. E., Offner, S. S. R., Parker, R. J., et al. 2015, *Nature*, 518, 213
- Pizzolato, N., Maggio, A., Micela, G., Sciortino, S., & Ventura, P. 2003, *A&A*, 397, 147
- Raghavan, D., McAlister, H. A., Henry, T. J., et al. 2010, *ApJS*, 190, 1
- Rayner, J. T., Toomey, D. W., Onaka, P. M., et al. 2003, *PASP*, 115, 362
- Reipurth, B. & Mikkola, S. 2012, *Nature*, 492, 221
- ROSAT Scientific Team. 2000, *VizieR Online Data Catalog*, IX/28A
- Rousset, G., Lacombe, F., Puget, P., et al. 2003, in Society of Photo-Optical Instrumentation Engineers (SPIE) Conference Series, Vol. 4839, Adaptive Optical System Technologies II, ed. P. L. Wizinowich & D. Bonaccini, 140–149
- Roy, A. & Haddow, M. 2003, *Celestial Mechanics and Dynamical Astronomy*, 87, 411
- Royer, F., Zorec, J., & Gómez, A. E. 2007, *A&A*, 463, 671
- Sana, H., Le Bouquin, J. B., Lacour, S., et al. 2014, *ApJS*, 215, 15
- Schröder, C. & Schmitt, J. H. M. M. 2007, *A&A*, 475, 677
- Siess, L., Dufour, E., & Forestini, M. 2000, *A&A*, 358, 593
- Skrutskie, M. F., Cutri, R. M., Stiening, R., et al. 2006, *AJ*, 131, 1163
- Thompson, T. A. 2011, *ApJ*, 741, 82
- Tokovinin, A. 2014, *AJ*, 147, 87
- Tokovinin, A. 2017, *MNRAS*, 468, 3461
- Tokovinin, A. 2018, *ApJS*, 235, 6
- Tokovinin, A. 2019, *AJ*, 158, 222
- Tokovinin, A. 2020, *MNRAS*, 496, 987
- Tokovinin, A., Thomas, S., Sterzik, M., & Udry, S. 2006, *A&A*, 450, 681
- Tokovinin, A. A. 1997, *A&AS*, 124, 75
- Toonen, S., Hamers, A., & Portegies Zwart, S. 2016, *Computational Astrophysics and Cosmology*, 3, 6
- Van Der Walt, S., Colbert, S. C., & Varoquaux, G. 2011, *Computing in Science & Engineering*, 13, 22
- van Leeuwen, F. 2007, *A&A*, 474, 653
- Waisberg, I. R. 2019, PhD thesis, LMU Munich, Germany
- Willez, J., Abad, J. A., Abuter, R., et al. 2019, *A&A*, 629, A41
- Zahn, J. P. 1977, *A&A*, 500, 121
- Zanazzi, J. J. 2021, arXiv e-prints, arXiv:2112.05868
- Zorec, J. & Royer, F. 2012, *A&A*, 537, A120

Table A.1. Individual radial velocities from literature.

Date (JD-2440000)	RV (km s ⁻¹)	source
2675.51	-21.0 ± 2.6	Nordstrom & Andersen (1985)
3262.82	-42.1 ± 1.4	Nordstrom & Andersen (1985)
3266.87	-9.7 ± 1.3	Nordstrom & Andersen (1985)
9615.51	3.92 ± 0.55	Grenier et al. (1999)

Table A.3. Individual radial velocities from SpeX.

Date (JD-2440000)	RV (km s ⁻¹)
17607.87	-33 ± 5
17610.82	-21 ± 5
17638.72	-16 ± 5
17898.98	31 ± 5
17903.10	-44 ± 5
17909.12	20 ± 5
17962.76	6 ± 5
17976.78	9 ± 5
17980.83	-7 ± 5
18009.81	-47 ± 5
18226.16	-31 ± 5
18257.98	3 ± 5
18342.72	4 ± 5
18374.73	-35 ± 5
18604.10	-38 ± 5
18615.98	-53 ± 5
18617.05	-18 ± 5
18979.97	-21 ± 5
19029.05	-35 ± 5
19032.80	-25 ± 5
19033.75	-26 ± 5

Table A.2. Individual radial velocities from FEROS.

Date (JD-2440000)	RV (km s ⁻¹)
13516.57	-28.28 ± 0.22
13516.61	-28.43 ± 0.07
13516.66	-27.97 ± 0.04
13516.71	-27.44 ± 0.04
13516.76	-27.21 ± 0.02
13516.82	-26.83 ± 0.04
13516.87	-26.37 ± 0.07
13516.91	-26.07 ± 0.22
13517.61	-21.26 ± 0.06
13517.66	-20.73 ± 0.07
13517.70	-20.27 ± 0.04
13517.76	-20.04 ± 0.04
13517.81	-19.51 ± 0.06
13517.86	-19.05 ± 0.06
13517.90	-18.37 ± 0.06
13518.60	-13.34 ± 0.07
13518.68	-12.42 ± 0.26
13915.49	-23.25 ± 0.13
13915.53	-24.24 ± 0.07
13915.57	-25.23 ± 0.07
13915.62	-26.37 ± 0.11

Appendix A: Tables

Table A.4. Positions of HIP 87813 used in the outer orbit fit.

Epoch	RA2000 (deg±mas)	DEC2000 (deg±mas)	source
1991.25	269.07933841 ± 0.34	-15.81236061 ± 0.25	<i>Hipparcos</i>
2000.00	269.079315 ± 10	-15.812520 ± 10	GSC2.3.2
2015.50	$269.0793072927252 \pm 0.10$	$-15.812841095549638 \pm 0.09$	<i>Gaia</i> DR2
2016.00	$269.07930698044726 \pm 0.09$	$-15.812851220033004 \pm 0.07$	<i>Gaia</i> eDR3